Solar Energy Materials & Solar Cells 227 (2021) 111014

Contents lists available at ScienceDirect

Solar Energy Materials and Solar Cells

journal homepage: http://www.elsevier.com/locate/solmat

Solid-state reaction process for high-quality organometallic halide perovskite thin film

Chien-Chung Hsu [a,2], Sheng-Min Yu [a,c,2], Kun-Mu Lee [d,e,f,2], Chuan-Jung Lin [a,2], Hao-Chien Cheng [b], Fu-Rong Chen [a,*,1]

[a] Department of Engineering and System Science, National Tsing Hua University, Hsinchu, 30013, Taiwan, ROC
[b] Department of Chemical and Materials Engineering, National Central University, Jhong-Li, 32001, Taiwan, ROC
[c] Material and Chemical Research Laboratories, Industrial Technology Research Institute, Chutung, Hsinchu, 31040, Taiwan, ROC
[d] Department of Chemical and Materials Engineering, Chang Gung University, Taoyuan, 33302, Taiwan
[e] Division of Neonatology, Department of Pediatrics, Chang Gung Memorial Hospital, Linkou, Taoyuan, 33305, Taiwan
[f] Green Technology Research Center, Chang Gung University, Taoyuan, 33302, Taiwan

ARTICLE INFO

Keywords:
In situ
$CH_3NH_3PbI_3$
Solid-solid reaction process (SSRP)
Roughness
Large grain

ABSTRACT

Recently, a hybrid perovskite material, ABX_3 (A= Cs, CH_3NH_3, NH_2CHNH_2; B= Pb, Sn; X= Cl, Br, I), has received much attention as an active layer in new-generation solar cells. This material is usually fabricated with either a one-step or a two step process in solution. However, the surface morphology, nucleation rate and grain growth rate of the $CH_3NH_3PbI_3$ perovskite light absorber prepared by the solution reaction process (SRP) are hard to control. Here, we show a fast solid-solid reaction process (SSRP), to fabricate ultraflat (roughness of approximately 12 nm) $CH_3NH_3PbI_3$ perovskite thin films with large grain sizes (~947 nm). The SSRP simply involves directly contacting a lead iodide thin film (PbI_2) with methylammonium iodide powder (CH_3NH_3I) without any chemical reagents at 120°C under a normal atmospheric environment. The SSRP reaction dynamics is investigated by an in situ heating scanning electron microscope (SEM) system. This innovative SSRP is an easy approach for the large-scale fabrication of planar heterojunction perovskite solar cells and allows us to demonstrate a power conversion efficiency of approximately 15.27% (active area of 0.16 cm^2).

1. Introduction

In recent years, perovskites (PVSK, $CH_3NH_3PbI_3$) have attracted attention for highly efficient solar cells [1,2] because they have excellent properties, with high absorption coefficients, long charge diffusion lengths, long carrier lifetimes [3–6], and fast bipolar transport [4]. PVSK solar cells can reach a conversion efficiency of 24.2% [7]. As a result, a perovskite/silicon solar tandem solar cell power conversion efficiency (PCE) of 25.2% can be achieved [8]. Usually, the fabrication process of PVSK films for solar cells involves either one-step [9] or two-step [10] reaction processes in solution (SRP).

In the one-step SRP [9], PbI_2 and methylammonium iodide (MAI, CH_3NH_3I) are dissolved together in dimethyl sulfoxide (DMSO) solution and then spin-coated onto a hole-transport material (HTM) substrate at 120°C to form a PVSK thin film. For the two-step SRP [10], PbI_2 and MAI are first individually dissolved in DMSO. Subsequentially, the two solutions are mixed in isopropanol (IPA) solutions. Then, similar to the one-step SRP, the final solution is spin coated at 120°C onto a hole-transport material. The device structure of PVSK solar cells can be either the mesoporous scaffold type [9] or planar heterojunction type [11]. It is known that the mesoporous scaffold type has several drawbacks; for instance, the precursor of the PVSK solution is difficult to fill into a mesoporous scaffold, leading to a low yield in mass production 1. In general, the surface morphology of PVSK thin films obtained from the SRP is hard to control due to the fast nucleation rate and fast grain growth rate of perovskite crystals, resulting in the formation of pinholes or discontinuous PVSK films [12]. In general, the SRP can be completed in 10 min, and the grain size and surface roughness of the PVSK obtained from the SRP are approximately 300 nm and 29.9 nm–40 nm, respectively. It is well acknowledged that the smaller surface roughness and

* Corresponding author.
E-mail address: frchen@me.com (F.-R. Chen).
[1] Fu-Rong Chen, Now is at Department of Materials Science and Engineering, City University of Hong Kong, Hong Kong.
[2] C. C. Hsu, S. M. Yu, K. M. Lee, and C.J. Lin contributed equally to this work and should be regarded as co-first authors.

https://doi.org/10.1016/j.solmat.2021.111014
Received 20 October 2020; Received in revised form 25 January 2021; Accepted 6 February 2021

larger grain size of PVSK films can greatly improve the efficiency of PVSK solar cells [13]. A good example shows that the contact resistance [14] between a smooth surface of the PVSK film and [6,6]-phenyl C61 butyric acid methyl ester (PCBM) can be greatly reduced. To improve the surface quality of PVSK films obtained from SRPs, a gas-induced formation/transformation (GIFT) process was proposed. GIFT utilizes the gas phase of CH_3NH_2 to react with a $CH_3NH_3PbI_3$ film grown after the SRP. Compared with the pure SRP, GIFT not only addresses the difficulty of filling a mesoporous scaffold but also avoids the formation of pinholes, which leads to improved surface roughness. GIFT usually gives results in PVSK films with a grain size and surface roughness of approximately 300 nm and 6 nm, respectively. A reasonably high efficiency of 15.1% [15,16] has been demonstrated via GIFT. Nevertheless, the stability of PVSK films obtained from SRPs is usually very poor because they can be easily and quickly decomposed in a highly moist environment [9]. Therefore, SRPs are usually conducted in a moisture-controlled glove box, which limits the possibility of utilizing SRPs as a mass production technique.

To improve the stability and reduce the density of pinholes to increase the efficiency of PVSK films, Snaith et al. [12] recently proposed a dual-source vacuum sublimation process (VSP) to grow a homogenous and pinhole-free PVSK film. The VSP in fact can be regarded as a gas phase process. A high-quality PVSK film with a large grain size of approximately 400 nm and a planar heterojunction-type surface roughness of approximately 22.4 nm was prepared by the VSP [12,17]. In 2016, Zhan'ao Tan developed a novel simplified close space sublimation (CSS) deposition process for growing a high-quality $CH_3NH_3PbI_3$ thin film in a low-vacuum and even nonvacuum oven [17]. This process involves using CH_3NH_3I (MAI) vapor to react with PbI_2 in a low vacuum environment. This chemical reaction took place in the gas phase, although it is similar to our solid-state reaction given in equation (1) and (Supplementary S1). The surface roughness and grain size can be more easily controlled with the VSP than with the one-step or two-step SRP because the rates of nucleation and grain growth are relatively slower. Conversely, slower nucleation and growth rates are drawbacks of the VSP since it usually takes approximately 1–2 h in a vacuum system; therefore, an extra thermal budget is needed for the VSP, which hinders its development toward a large-scale process.

Thermodynamically, the reaction of MAI and PbI_2 is similar in both vapor phase [17–21] and solid state. We believed that the SSRP and the VSP process can taken place simultaneously, since they are all energetically favorable in both gas phase and solid state (equation (1) and supplementary S1). Kinetics of this reaction can speed up in the solid state due to higher contact density of MAI with PbI_2 (supplementary S2). Besides, the solid state reaction of MAI and PbI_2 is allowed to operate at normal ambient, 1atm. A comparison table between the VSP [12,17–21] and solid state reaction is given in Supplementary Table 1). To use the roll-to-roll process to achieve high-quality PVSK films with smaller roughness and larger grain size, we report an efficient solid-solid reaction process (SSRP) at 120°C in an atmospheric environment to grow uniform PVSK films. In this work, the reaction dynamics of SSRP between MAI and PbI_2 was first time observed with an in-situ heating SEM by taking time-resolved snapshots. In the SEM, later it will be shown the solid state reaction can take place locally at the interface of MAI/PbI_2, and also at the same time the sublimation of MAI concurrently occurs. This SSRP allows the PVSK film to have large grains with sizes of approximately 950 nm and a small surface roughness of approximately 12 nm. This process has hitherto not been reported elsewhere. In our SSRP, the PVSK film was formed by a solid-state reaction of PbI_2 and MAI (CH_3NH_3I) powder. Compared with the SRP, the VSP, CCS and GIFT, our SSRP is not required to operate in a glove box; therefore, mass production of PVSK solar cells can be implemented over a large area with a roll-to-roll process under a normal atmospheric environment. In general, the grain size and surface roughness of the PVSK thin film processed via the SSRP are much better than those resulting from the SRP. In this paper, we demonstrate that a solid-state processed PVSK film has an extremely large grain size of approximately 950 nm and a surface roughness of approximately 10 nm and guarantees the best conversion efficiency of up to 15.27% (active area 0.16 cm^2), with a lifetime of 1200 h. X-ray diffraction (XRD), photoluminescence spectroscopy (PLS), atomic force microscopy (AFM), transmission electron microscopy (TEM) and scanning electron microscope (SEM) were used to analyze the structural evolution and characterize the properties of the PVSK film after processing via solid-state reaction. The SSRP mechanism will be discussed in detail in a later section.

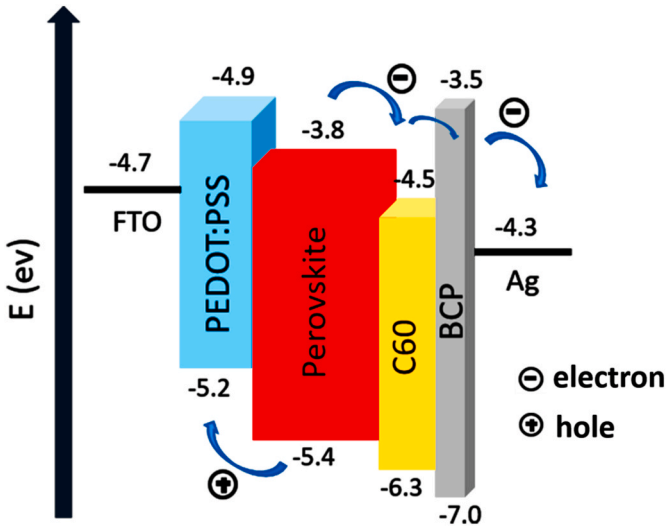

Fig. 1. Schematic representation of an energy band diagram of our perovskite device composed of the layered stacked FTO/PEDOT/Perovskite/C_{60}/BCP/Ag structure (⊕ hole; ⊖ electron).

2. Experimental

2.1. Device structure and fabrication

An inverted planar heterojunction PVSK solar cell composed of layer stacked structured FTO/PEDOT/PVSK film/C_{60}/bathocuproine (BCP)/Ag is shown in Fig. 1. The PVSK film is prepared by the SSRP. The work function of each layer is also given in Fig. 1. When the active layer of the PVSK film absorbs a photon, the electron is pumped from the valence band to the conduction band. The electrons are then transported to neighboring layered n-type C_{60}, which plays a role as an electron transport layer (ETL). The ETL has a lower work function (−4.5 eV) that matches the lowest unoccupied molecular orbital (LUMO) energy level of the PVSK film, which further accelerates electron transport toward the silver cathode. The role of bathocuproine (BCP) is to prevent the holes transmitted to the Ag cathode from being annihilated with electrons. The work function of FTO/PEDOT:PSS must be matched with the highest molecular orbital (HOMO) energy level of FTO to effectively guide the holes. The p-type PEDOT:PSS film is a hole transport layer (HTM) that modifies the work function (−4.9 eV) of FTO to prevent electron injection toward the anode and improve the efficiency of the hole.

The processing procedures are given schematically in Fig. 2a. The FTO substrate was first ultrasonically cleaned with chemical reagents including neutral detergent, ethanol, acetone, isopropanol, and DI water. The cleaning time for each reagent was 10 min. Finally, the FTO substrate was dried by N_2 gas in an oven at 120°C for 30 min to confirm the removal of residual water. A PEDOT:PSS (Clevios PVP AI-4083) HTM thin film with a thickness of 40 nm is prepared by spin-coating at a speed of 5000 revolutions per minute (rpm) for 50 s. The HTM film is then annealed at 120°C for 10 min. A 200 nm-thick flat PbI_2 coating is then applied with a spin-coater at a speed of 6000 rpm for 10 s.

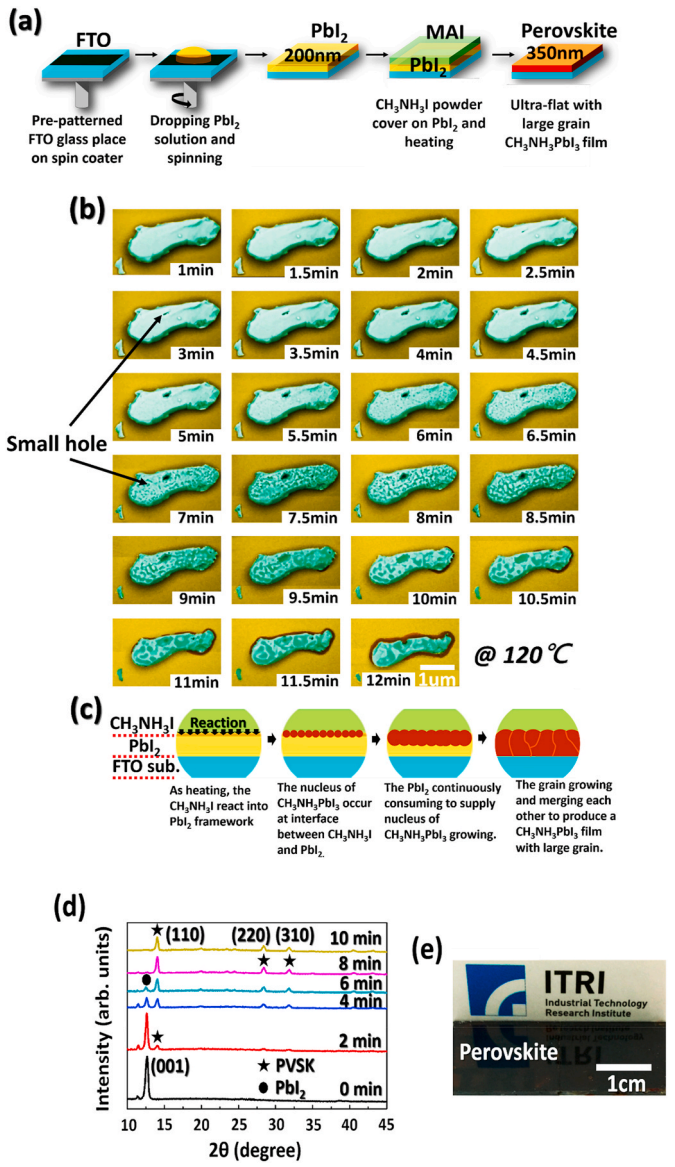

Fig. 2. (a) Schematic diagram showing the procedures of the SSRP. (b) In situ heating experiment used to evaluated the SSRP with a desktop SEM system. The gold, green, and brown colors represent PbI_2, CH_3NH_3I, and $CH_3NH_3PbI_3$, respectively. The scale bar is equal to 1 μm; (c) The reaction mechanism proposed for the SSRP. (d) XRD diffraction patterns at different reaction times. After 4 min, the phase transition to the initial PVSK phase (★ PVSK; ● PbI_2) is clearly shown. (e) Large-area (4 cm × 2 cm) $CH_3NH_3PbI_3$ film fabricated by the SSRP on a glass substrate (black area). (For interpretation of the references to color in this figure legend, the reader is referred to the Web version of this article.)

Interestingly, the crystalline PVSK film can be formed via direct contact of $PbI_{2(s)}$ and CH_3NH_3I ($MAI_{(s)}$) in the solid-state, even without dissolving PbI_2 and MAI in the solution. The details of the solid-state reaction used for the growth of the perovskite film are given as follows. The as-coated PbI_2 film was annealed at 120°C for 10 min. The CH_3NH_3I (MAI) powder was prepared according to reported procedures [22] with some modifications (Supplementary S1). The CH_3NH_3I (MAI) power is then uniformly covered on the top of the PbI_2 film (Fig. 2a). The temperature-dependent free energy of formation of PVSK is given as follows:

$$CH_3NH_3I_{(S)} + PbI_{2(s)} \longrightarrow CH_3NH_3PbI_{3(s)},\ G^o = -359.53T\text{-}554.26 \quad \ldots\ldots \quad (1)$$

Here, a = −359.53, and b = −554.26. At room temperature of 298 K, G = −107694.21 (kJ/mol) [23].

Basically, this solid-state reaction can already take place spontaneously at room temperature based on equation (1), but to speed up the reaction rate, the stack of the PbI_2 film and MAI powder is treated with thermal reaction at 120°C for 0–10 min (Fig. 2a). After completion of the above solid-state reaction, the residual CH_3NH_3I (MAI) powder is removed with the following procedures: tilting sample and using inert gas to remove MAI, or even using a soft brush. Then, thin layers of C_{60}/BCP with thicknesses of 45 nm and 5 nm are deposited onto perovskite films formed by the above solid-state reaction. A 100 nm-thick Ag metal contact is coated using a thermal evaporator for the final step of device fabrication. The active areas of the small- and large-area devices are 0.16 cm^2 and 11.25 cm^2, respectively. The area of the solar cell was defined by using a shadow mask during Ag evaporation.

2.2. Equipment specification

An in-situ heating SEM system EM-100 manufactured by TEMIC Ltd, Taiwan was used for reaction dynamics of SSRP process. An excitation wavelength of 633 nm was used for the photoluminescence (PL) (Agilent Technologies) experiment. The photocurrent density and voltage (J-V) curves were measured using a computer-controlled digital source meter (Keithley 2400) under 1 sun illumination (100 mW/cm^2, AM1.5G). The solar simulator used was an Oriel Sol3A class AAA simulator. A 450 W xenon lamp (Newport 6279NS) was used as a light source. The light intensity was calibrated using an NREL-certified silicon solar cell (Oriel, 91150 V) with a KG-5 filter before each measurement [24]. During the measurement, the device was covered with a metal mask with aperture areas of 0.16 cm^2 and 11.25 cm^2. The voltage scan rate was fixed at 50 mV/s.

3. Results and discussion

An in-situ heating SEM was first time implemented for observing the dynamics of SSRP reaction. The SEM images in Figure 2b show the dynamic reaction between MAI and PbI_2 at 120 °C. PbI_2, CH_3NH_3I (MAI), and $CH_3NH_3PbI_3$ (PVSK) are gold, green, and brown, respectively, in Fig. 2b. From Figure 2b, the topology evolution during the SSRP is recorded in snapshots every 30 s. The appearances of PbI_2 and CH_3NH_3I do not significantly change until the SSRP time is longer than 2 min. At a treatment time of 2.5 min, a small hole starts appearing on the CH_3NH_3I surface (green area), indicating that sublimation of CH_3NH_3I (MAI) begins and also to react with PbI_2. The diameter of this hole increases with prolonged SSRP treatment time. By further extending the treatment time to 5.5 min, the surface morphology of CH_3NH_3I starts changing. Toward the end, the green area significantly shrinks, indicating that a noticeable amount of CH_3NH_3I is consumed from 5.5 min to 10 min. This is an indication that vapor phase reaction may be possible at the same time of the local The SSRP is expected to take place locally at the interface of PbI_2 and CH_3NH_3I. As sated in the experimental section, the CH_3NH_3I (MAI) power is then uniformly spread on the top of the PbI_2 film (Fig. 2a). At the initial stage of reaction, the $CH_3NH_3PbI_3$ nucleates at the interface of MAI and PbI_2. But since the snapshot of SEM image can only be recorded from top view therefore information of lateral growth of $CH_3NH_3PbI_3$ nucleus is hindered under the CH_3NH_3I (MAI). The $CH_3NH_3PbI_3$ film cannot be revealed until the top layer of CH_3NH_3I (MAI) is partially consumed. The phase is fully transitioned in 10 min via the SSRP, which is consistent with the XRD results. Based on in situ heating SEM results, the reaction mechanism of the SSRP can be divided into four stages, schematically shown in Fig. 2c.

(I) As the heating treatment starts, the MAI powders can spontaneously react with PbI_2 according to equation (1);
(II) The nucleus of PVSK uniformly forms at the interface between MAI and PbI_2.

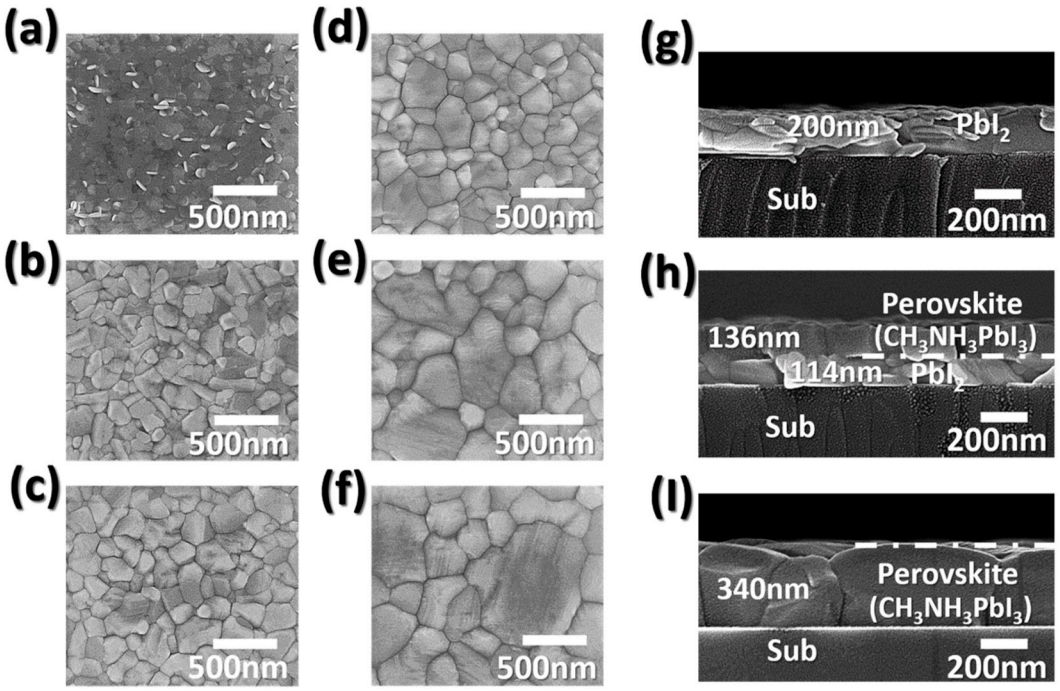

Fig. 3. Structural evolution during the SSRP. (a)–(f) SEM images showing the surface morphology from the top view. (a) PbI_2 film prepared with reaction times of (b) 2 min, (c) 4 min, (d) 6 min, (e) 8 min, and (f) 10 min. (g) to (i) SEM images showing the corresponding cross-sectional view at (g) 0 min, (h) 4 min, and (i) 10 min, respectively.

(III) 2D lateral growth of PVSK occurs by continuously consuming CH_3NH_3I and PbI_2.

The 2D growth mode of the PVSK film will be confirmed from the analysis of the lateral and depth growth rates in Fig. 3. The 2D growth mode will be proven from the lateral and longitudinal growth rates in a later section.

(IV) The final PVSK film forms by the impingement of many 2D-grown grains.

The structural evolution of the PVSK film by the SSRP was characterized using X-ray diffraction (Fig. 2d) and a high-resolution transmission electron microscope (JEOL 2010F), while the surface morphology of the PVSK film and cross-sectional stacking structure of the device were investigated using a high-resolution field emission scanning electron microscopy (FE-SEM) system JSM-7600F, JOEL) (Fig. 3). AFM was also implemented to support the analysis of surface roughness. Here, we show that the SSRP is a novel method for fabricating ultraflat PVSK films with grain sizes as large as approximately 974 nm and a roughness of approximately 10 nm.

3.1. Characterization

The crystal structure of the as-synthesized PVSK film was determined using X-ray diffraction equipped with Cu-Kα radiation, and data were collected with a scan rate of 2° per minute under operating conditions of 45 kV and 35 mA. Fig. 2d shows the X-ray diffraction pattern of PVSK films prepared by the SSRP at different reaction treatment times. It is evident that the solid-state reaction resulting in a phase transition at 120°C to form PVSK may start as early as 2 min. Before the SSRP, the strong diffraction peak of PbI_2 at 12.67° is consistent with the {001} peak of the PbI_2 hexagonal phase given in the standard database (JCPD card #07–0235) [25]. This suggests that PbI_2 presents a strong <001> texture in the hexagonal polycrystalline phase. After 2 min of the SSRP, the X-ray pattern shows that the {001} peak of PbI_2 becomes weaker, accompanied by the appearance of three new extra diffraction peaks at 14.10°, 28.44°, and 31.80°. They are assigned as the {110}, {220}, and {310} peaks of the tetragonal structure of PVSK and are in good agreement with those reported in earlier publications [12]. This provides evidence that the pristine hexagonal phase of the PbI_2 thin film has been converted to the tetragonal crystal structure of PVSK during the SSRP [10,12,26]. Note that for the spectra recorded from 2 min to 6 min, a weak diffraction peak near 18° can be assigned as the {101} peak of CH_3NH_3I (MAI), indicating that the SSRP may not be completed [26]. In general, the crystalline $CH_3NH_3PbI_3$ phase starts to appear at 2 min. As the SSRP is prolonged, the intensity of the diffraction peaks associated with the PVSK phase at identical positions increases, while the diffraction intensity associated with the PbI_2 structure decreases with extension of the reaction time. By prolonging the SSRP to 8–10 min, the diffraction peaks associated with PbI_2 and CH_3NH_3I completely disappear, suggesting that the PbI_2 film has fully transformed to a $CH_3NH_3PbI_3$ PVSK film. Compared to conventional processes, including one-step and two-step reactions in solution [10] and vapor-assisted [12] and gas-assisted processes [15,16], the SSRP has several advantages in terms of cost reduction and short processing time. First, the reaction time of SSRPs is comparable to that of SRPs and is certainly much faster than that of VSPs. The reaction time needed for the gas phase (VRP) is usually approximately 1–2 h [12] and approximately 13 min [16] for the solution processes. Note that SSRPs can be carried out under normal ambient conditions without a vacuum system, and the significantly reduced production cost is due to CH_3NH_3I powder being recycled. Furthermore, no solvents or reagents, such as toluene, chlorobenzene, etc., are used in SSRPs, which avoids posttreatment of the waste solution and is expected to simplify the $CH_3NH_3PbI_3$ (PVSK) film fabrication process.

The SEM images in Fig. 3a–f display the evolution of the surface morphology at 2-min intervals during the solid-state reaction of MAI with the PbI_2 film. We can see that the grains of the perovskite film grow from 212 nm ± 20 nm (at 2 min, Fig. 3b) to 947 nm ± 20 nm (at 10 min at Fig. 3f). The lateral growth rate is estimated from Fig. 3b–f to be 1.57 nm/s. Fig. 3g to l show the structural evolution in a cross-sectional view

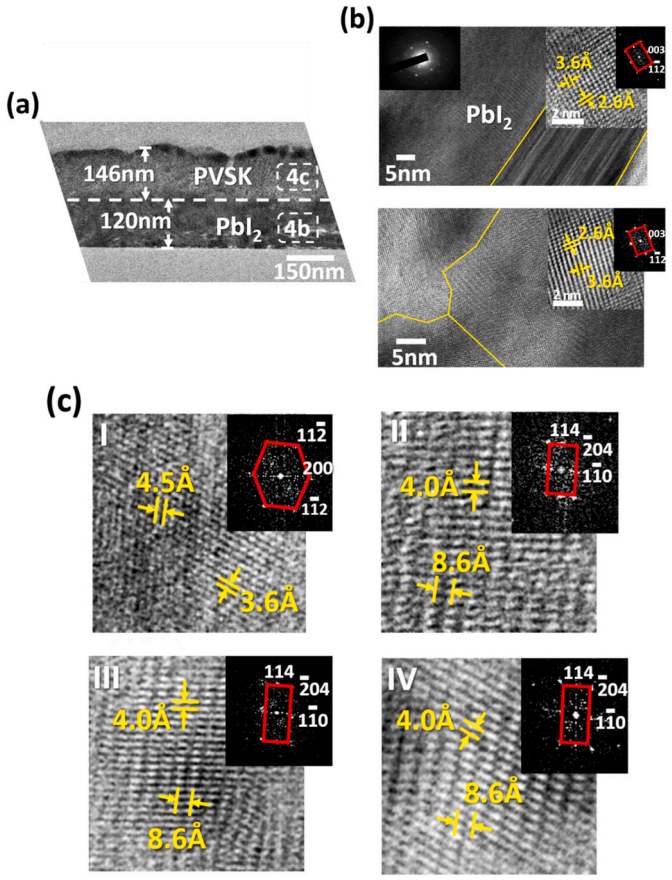

Fig. 4. (a) HRTEM image showing the two-layer structure of the film processed via the SSRP for 4 min. (b) Magnified view of PbI2. Inset showing the zone axis top: $[110]_{hex}$, bottom: $[110]_{hex}$. (c) HRTEM images showing that the $CH_3NH_3PbI_3$ perovskite has a tetragonal structure. Zone axis of the inset FT pattern I: $[021]_{tet}$, II: $[221]_{tet}$, III:$[221]_{tet}$ and IV:$[221]_{tet}$.

at different treatment times, 0, 4 and 10 min. As suggested from XRD, the SSRP is completed at 10 min. Fig. 3i (10 min) shows that the thickness of $CH_3NH_3PbI_3$ in the perovskite layer reaches approximately 340 nm. Note that the grains extend through the whole film and have a size consistent with that determined from the planar view of approximately 947 nm in Fig. 3f. It can be seen that not only does the grain size increase but the film also becomes thicker, with the thickness increasing from 200 to 340 nm as the treatment time increases. The growth rate in the longitudinal direction is estimated to be 0.56 nm/s, which is approximately 1/3 of the growth rate in the lateral direction. This suggests that the SSRP favors a 2D growth mode for PVSK films. Together with the evidence of the uniform grain size (±20 nm, Fig. 3b–f), it is reasonably envisaged that a homogeneous distribution of perovskite nuclei form heterogeneously and then grow on the entire interface of PbI_2 and CH_3NH_3I powder during the SSRP.

The structure in Fig. 3h is that of a sample treated for 4 min, which shows a two-layer structure above the substrate. This is consistent with the XRD results in Fig. 2d. According to the XRD pattern in Fig. 2d, the SSRP is incomplete at 4 min, and we expect to see a mixture of perovskite/PbI_2 film (Fig. 3h). The two-layer structure shows a thickness of 250 ± 20 nm in Fig. 3h, which is also confirmed by TEM observation (Fig. 4a) of the same sample. Fig. 4a shows a sharp interface between the perovskite (thickness ~146 nm) and PbI_2 (thickness ~120 nm) films. The crystal structure of both the PVSK and PbI2 phases can be confirmed from the Fourier transforms (FTs) of the local atomic-resolution images from the areas enclosed by white circles. The magnified views of the HRTEM images of the PbI_2 and PVSK films in these two areas are given in Fig. 4b and c, respectively. From the FTs, we see that PVSK and PbI_2 are tetragonal structures and hexagonal structures, respectively. These results are consistent with the XRD results. The crystallographic orientation and indices are given in the figure caption.

Photoluminescence spectroscopy is a tool that can independently offer information on structural evolution, e.g., the formation of the PVSK film during the SSRP. In Fig. 5a, the perovskite film has a PL peak at a wavelength of 761 nm, which corresponds to a band gap of 1.6 eV. We observed that the PL intensity increased for the samples treated with longer reaction times. The increase in the PL intensity basically attributes from two causes. First, the photo-excited carriers can be recombined at the residual PbI_2 layer [27,28] so that the PL intensity is relatively weak for the reaction time shorter than 10 min. Second, it gives evidence that the amount of perovskite increases as it shown in the XRD spectrum (Fig. 2d).

The evolution of surface roughness in the SSRP can be analyzed using three-dimensional time-resolved atomic force microscopy (3D-AFM). As seen in Figure 5b to g, the 3D-AFM images show the root mean square values of roughness for the thin film prepared by the SSRP at 0, 2, 4, 6, 8,

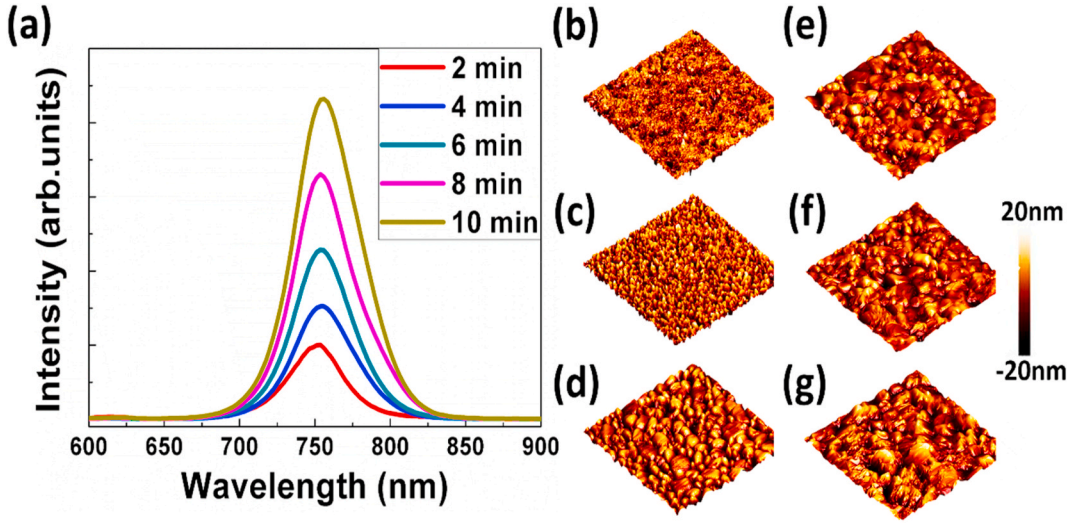

Fig. 5. (a) Photoluminescence spectrum of the samples treated at various reaction times. (b)–(g) Surface roughness analysis of thin films treated by SSRPs performed using 3D AFM at different treatment times: (b) 0 min, pure PbI_2; (c) 2 min; (d) 4 min; (e) 6 min; (f) 8 min; and (g) 10 min. The surface roughness (*Rms*) values are 9.3 nm, 9.8 nm, 10.5 nm, 10.8 nm, 11.3 nm and 11.8 nm. Scale size is 5 μm × 5 μm.

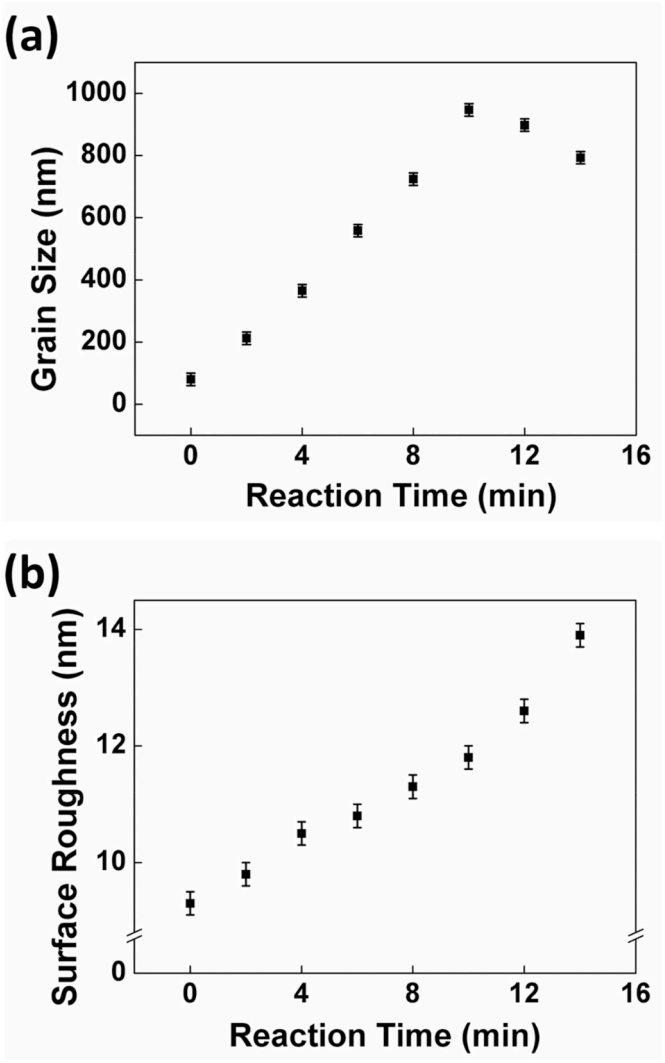

Fig. 6. (a) and (b), the relationship of grain size and surface roughness of PVSK films reaction for different times: 0 min (pure PbI_2), 2 min, 4 min, 6 min, 8 min, 10 min, 12 min and 14 min of the SSRP.

10, 12 and 14 min. The roughness values are 9.3 nm, 9.8 nm, 10.5 nm, 10.8 nm, 11.3 nm, 11.8 nm, 12.5 nm and 14 nm with error bars of ±0.2 nm. Some earlier works [29,30] have demonstrated prolongation of the reaction time in the one-step can increase the grain size. However, the situation is quite different in the solid state reaction process (SSRP). In SSRP, MAI is the top upper layer on PbI_2. It completely reacts to perovskite in 10 min, in Figs. 2b and Fig. 3. As it is known that grain size of think film usually is limited by the thickness of thin film. Our experiment showed prolongation of the treatment time beyond 10 min, the grain slightly shrinks and the surface roughness gets worse. Before 10 min, the surface roughness (Fig. 6) increases linearly with grain size, which is implicitly attributed to the impingement of grains from the 2D grain growth mode. However, the surface roughness increases with prolonged SSRP treatment time may be due to formation of deeper grain boundary groves. After all, the surface roughness of 14 nm at 14 min obtained via the SSRP is flatter than the reported roughness of 40 nm obtained via the SRP [31,32].

It has been reported that in general, a flatter surface gives better contact resistance [33,34]. The extremely flat surface of the PVSK film prepared by the SSRP can improve the contact resistance with C_{60}/BCP to reduce the series resistance (Rs). The contact resistance we measured for the samples treated at 10 min is Rs = 16.2 ± 0.2 Ω·cm^2, which is far smaller than Rs = 61.1 ± 2.6 Ω·cm^2, which is the contact resistance of

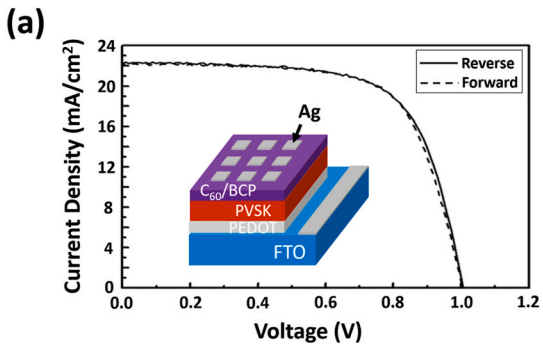

Reverse	Voc (V)	Jsc (mA/cm²)	F.F (%)	Efficiency (%)	Forward	Voc (V)	Jsc (mA/cm²)	F.F (%)	Efficiency (%)
Champion	1.01	22.20	68.08	15.21	Champion	1.00	22.16	68.65	15.27
Avg.	1.02	19.04	64.71	12.55	Avg.	1.02	18.93	66.58	12.80
STD.	0.01	1.29	1.66	1.05	STD.	0.01	1.36	1.43	1.03

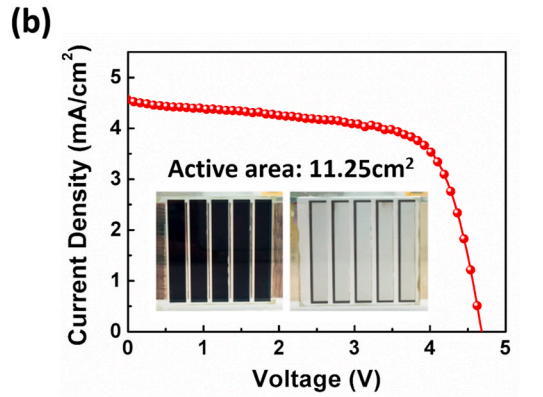

I_{sc} (mA)	J_{sc} (mA/cm2)	V_{oc} (V)	F.F	Efficiency (%)
42.72	4.52	4.685	0.683	14.46

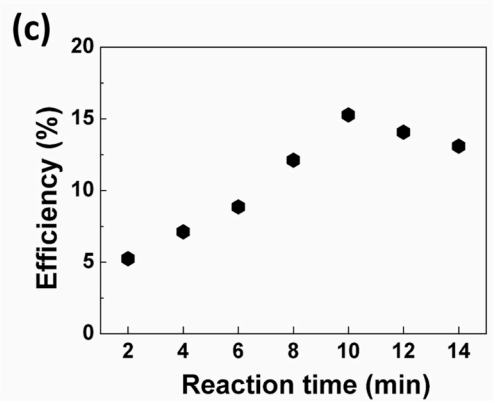

Fig. 7. (a) The current density-voltage curve and parameters; (b) photograph of a perovskite solar cell with an active area of 25 cm^2 (c) The power conversion efficiency of SSRP device as a function of processing time.

the film processed by solution treatment [35].

Based on the above results, a solar cell device is prepared using the PVSK film processed at all different times, 2, 4, 6, 8, 10, 12 and 14 min. The photovoltaic performance for a short circuit density (*Jsc*) of 22.16 mA/cm^2, open-circuit voltage (Voc) of 1 V and fill factor (FF) of 68.65% gives a power conversion efficiency (PCE) of 15.27% (active area of 0.16 cm^2) in Fig 7a. On the other hand, we achieved a submodel perovskite solar cell (25 cm^2) with a PCE of 14.46% (active area of 11.25 cm^2), as shown in Fig. 7b. Fig. 7c shows the conversion efficiencies of the film are 5.25%, 7.12%, 8.87%, 12.11%, 15.27%. 14.25%, and 13%, after

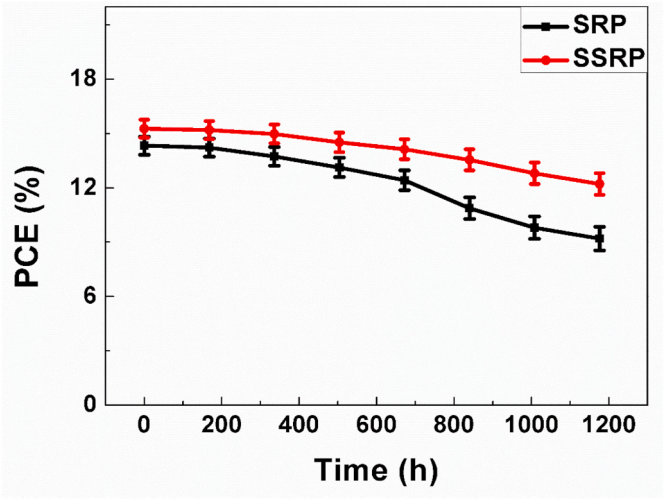

Fig. 8. The long-term stability in efficiency of perovskite photovoltaic cells fabricated from the solution reaction process (SRP) and solid-state reaction process (SSRP) was tested for 1200 h. The efficiency was tested at 40% relative humidity (RH) and 25°C.

reaction at different times, 2, 4, 6, 8, 10, 12 and 14 min, respectively. The highest efficiency of our perovskite device is at processing time of 10 min. Our experimental evidences shows the prolongation of processing time beyond 10 min may cause conversion efficiency decreases which is in the same trend of the grain size. The long-term stability in the efficiency of perovskite photovoltaic cells fabricated from the solution reaction process (SRP) and solid-state reaction process (SSRP) are shown in Fig. 8. These devices were tested at 40% relative humidity (RH) and 25°C. In general, the efficiency obtained via the SSRP is always superior to that obtained via the SRP. After 1200 h, the efficiencies of the perovskite photovoltaic cells fabricated from the SSRP and SRP decay to 19% and 35.7% of their initial efficiencies, respectively.

4. Conclusions

In conclusion, an innovative solid-state process is demonstrated for fabricating high-quality organometallic halide perovskite thin films with larger grain sizes (~947 nm) and flatter surfaces (~12 nm), resulting in films that are superior to those obtained by traditional solution processes. A solar cell device is prepared and demonstrated to have a power conversion efficiency of approximately 15.27% (active area 0.16 cm^2). The efficiency of a perovskite depends on many factors and can be improved through many other routes. Although this efficiency is comparable to that obtained with the traditional solution process, the most important novelty of our SSRP reported here is that the SSRP can be carried out under a normal atmospheric environment without involving a wet bench or glove box, which facilitates the possibility of obtaining a roll-to-roll solution for mass production and reduces costs.

CRediT authorship contribution statement

Chien-Chung Hsu: Writing – original draft, Validation, Methodology, Conceptualization. **Sheng-Min Yu:** Resources, Methodology. **Kun-Mu Lee:** Resources, Validation, Methodology. **Chuan-Jung Lin:** Methodology, Conceptualization. **Hao-Chien Cheng:** Validation. **Fu-Rong Chen:** Supervision, Writing – review & editing, Writing – original draft, Conceptualization.

Declaration of competing interest

The authors declare that they have no known competing financial interests or personal relationships that could have appeared to influence the work reported in this paper.

Acknowledgments

This work was supported by the Ministry of Science and Technology, Taiwan (Grant Number: MOST 108-2628-E-182-003-MY3), Chang Gung University (QZRPD181) and Chang Gung Memorial Hospital, Linkou, Taiwan (CMRPD2G0301 and CMRPD2G0302). FRC also would like to acknowledge the support from MOST-105-2221-E-007-023-MY3, MOST 104-2221-E-007-067-MY3 and City University of Hong Kong under projects of project number 9360162 and 9380092.

Appendix A. Supplementary data

Supplementary data to this article can be found online at https://doi.org/10.1016/j.solmat.2021.111014.

References

[1] Z.K. Tan, R.S. Moghaddam, M.L. Lai, P. Docampo, R. Higler, F. Deschler, M. Price, A. Sadhanala, L.M. Sadhanala, D. Credgington, F. Hanusch, T. Bein, H.J. Snaith, R. H. Friend, Bright light-emitting diodes based on organometal halide perovskite, Nat. Nanotechnol. 9 (2014) 687–692, https://doi.org/10.1038/nnano.2014.149.
[2] N. Islam, M. Yang, K. Zhu, Z. Fan, Mesoporous scaffolds based on TiO_2 nanorods and nanoparticles for efficient hybrid perovskite solar cells, J. Mater. Chem. A 3 (2015) 24315–24321, https://doi.org/10.1039/C5TA06727H.
[3] H.S. Kim, C.R. Lee, J.H. Im, K.B. Lee, T. Moehl, A. Marchioro, S.J. Moon, R. Humphry-Baker, J.H. Yum, J.E. Moser, M. Grätzel, N.G. Park, Lead iodide perovskite sensitized all-solid-state submicron thin film mesoscopic solar cell with efficiency exceeding 9%, Sci. Rep. 2 (2012) 591, https://doi.org/10.1038/srep00591.
[4] J.H. Heo, S.H. Im, J.H. Noh, T.N. Mandal, C.S. Lim, J.A. Chang, Y.H. Lee, H.J. Kim, A. Sarkar, M.K. Nazeeruddin, M. Grätzel, S.I. Seok, Efficient inorganic–organic hybrid heterojunction solar cells containing perovskite compound and polymeric hole conductors, Nat. Photon. 7 (2013) 486–491, https://doi.org/10.1038/nphoton.2013.80.
[5] S.D. Stranks, G.E. Eperon, G. Grancini, C. Menelaou, M.J.P. Alcocer, T. Leijtens, L. M. Herz, A. Petrozza, H.J. Snaith, Electron-hole diffusion lengths exceeding 1 micrometer in an organometal trihalide perovskite absorber, Science 342 (2013) 341–344, https://doi.org/10.1126/science.1243982.
[6] G. Xing, N. Mathews, S. Sun, S.S. Lim, Y.M. Lam, M. Grätzel, S. Mhaisalkar, T. C. Sum, Long-Range.Balanced electron- and hole-transport lengths in organic-inorganic $CH_3NH_3PbI_3$, Science 342 (2013) 344–347, https://doi.org/10.1126/science.1243167.
[7] K. Xiao, P. Lin, Q. Han, Y. Hou, Z. Qin, H.T. Nguyen, J. Wen, M. Wei, V. Yeddu, M. I. Saidaminov, Y. Gao, X. Luo, Y. Wang, H. Gao, C. Zhang, J. Xu, J. Zhu, E. H. Sargent, H. Tan, All-perovskite tandem solar cells with 24.2% certified efficiency and area over 1 cm^2 using surface-anchoring zwitterionic antioxidant, Nat. Energy 5 (2020) 870–880, https://doi.org/10.1038/s41560-020-00705-5.
[8] F. Sahli, J. Werner, B.A. Kamino, M. Bräuninger, R. Monnard, B.P. Salomon, L. Barraud, L. Ding, J.J. Diaz Leon, D. Sacchetto, G. Cattaneo, M. Despeisse, M. Boccard, S. Nicolay, Q. Jeangros, B. Niesen, C. Ballif, Fully textured monolithic perovskite/silicon tandem solar cells with 25.2% power conversion efficiency, Nat. Mater. 17 (2018) 820–826, https://doi.org/10.1038/s41563-018-0115-4.
[9] A. Kojima, K. Teshima, Y. Shirai, T. Miyasaka, Organometal halide perovskites as visible-light sensitizers for photovoltaic cells, J. Am. Chem. Soc. 131 (2009) 6050–6051, https://doi.org/10.1021/ja809598r.
[10] J. Burschka, N. Pellet, S.J. Moon, R. Humphry-Baker, P. Gao, M.K. Nazeeruddin, M. Grätzel, Sequential deposition as a route to high-performance perovskite-sensitized solar cells, Nature 499 (2013) 316–320, https://doi.org/10.1038/nature12340.
[11] T. Leijtens, G.E. Eperon, S. Pathak, A. Abate, M.M. Lee, H.J. Snaith, Overcoming ultraviolet light instability of sensitized TiO_2 with meso-superstructured organometal tri-halide perovskite solar cells, Nat. Commun. 4 (2013) 2885, https://doi.org/10.1038/ncomms3885.
[12] M. Liu, M.B. Johnston, H.J. Snaith, Efficient planar heterojunction perovskite solar cells by vapour deposition, Nature 501 (2013) 395, https://doi.org/10.1038/nature12509.
[13] Z. Liang, S. Zhang, X. Xu, N. Wang, J. Wang, X. Wang, Z. Bi, G. Xu, N. Yuan, J. Ding, A large grain size perovskite thin film with a dense structure for planar heterojunction solar cells via spray deposition under ambient conditions,, RSC Adv. 5 (2015) 60562–60569, https://doi.org/10.1039/C5RA09110A.
[14] S. Collavini, M. Saliba, W.R. Tress, P.J. Holzhey, S.F. Völker, K. Domanski, S. H. Turren-Cruz, A. Ummadisingu, S.M. Zakeeruddin, A. Hagfeldt, M. Grätzel, J. L. Delgado, Poly(ethylene glycol)–[60]Fullerene-based materials for perovskite solar cells with improved moisture resistance and reduced hysteresis, ChemSusChem 11 (2018) 1032–1039, https://doi.org/10.1002/cssc.201702265.
[15] Y. Zhou, N.P. Padture, Gas-induced formation/Transformation of organic–inorganic halide perovskites, ACS Energy Lett. 2 (2017) 2166–2176, https://doi.org/10.1021/acsenergylett.7b00667.

[16] Z. Zhou, Z. Wang, Y. Zhou, S. Pang, D. Wang, H. Xu, Z. Liu, N.P. Padture, G. Cui, Methylamine-gas-induced defect-healing behavior of $CH_3NH_3PbI_3$ thin films for perovskite solar cells, Angew. Chem. Int. 54 (2015) 9705–9709, https://doi.org/10.1002/anie.201504379.

[17] Q. Guo, C. Li, W. Qiao, S. Ma, F. Wang, B. Zhang, L. Hu, S. Dai, Z. Tan, The growth of a $CH_3NH_3PbI_3$ thin film using simplified close space sublimation for efficient and large dimensional perovskite solar cells,, Energy Environ. Sci. 9 (2016) 1486–1494, https://doi.org/10.1039/C5EE03620H.

[18] W. Jin, X. Zou, X. Bai, Y. Yang, D. Chen, CH_3NH_3I treatment temperature of 70 °C in low-pressure vapor-assisted deposition for mesoscopic perovskite solar cells, Chem. Phys. Lett. 691 (2018) 444–448, https://doi.org/10.1016/j.cplett.2017.11.058.

[19] L. Gu, S. Wang, X. Fang, D. Liu, Y. Xu, N. Yuan, J. Ding, High-performance large-area perovskite solar cells enabled by confined space sublimation, ACS Appl. Mater. Interfaces 12 (2020) 33870–33878, https://doi.org/10.1021/acsami.0c10830.

[20] E. Pérez-Gutiérrez, M.J. Percino, D.M. Montoya, D. Solis-Ibarra, M. Cerón, O. Barbosa-García, Control of the morphology and crystallinity of a PbI_2 layer for large-area perovskite films prepared by close space sublimation, ACS Appl. Energy Mater. 1 (2018) 3843–3849, https://doi.org/10.1021/acsaem.8b00610.

[21] L. Chen, F. Tang, Y. Wang, S. Gao, W. Cao, J. Cai, L. Chen, Facile preparation of organometallic perovskite films and high-efficiency solar cells using solid-state chemistry, Nano Res. 8 (2015) 263–270, https://doi.org/10.1007/s12274-014-0662-1.

[22] G.E. Eperon, V.M. Burlakov, P. Docampo, A. Goriely, H.J. Snaith, Morphological control for high performance, solution-processed planar heterojunction perovskite solar cells, Adv. Funct. Mater. 24 (2014) 151–157, https://doi.org/10.1002/adfm.201302090.

[23] G.P. Nagabhushana, R. Shivaramaiah, A. Navrotsky, Direct calorimetric verification of thermodynamic instability of lead halide hybrid perovskites, Proc. Indian Nat. Sci. Acad. 113 (2016) 7717–7721, https://doi.org/10.1073/pnas.1607850113.

[24] K.M. Lee, C.J. Lin, B.Y. Liou, S.M. Yu, C.C. Hsu, V. Suryanarayanan, M.-C. Wu, Selection of anti-solvent and optimization of dropping volume for the preparation of large area sub-module perovskite solar cells, Sol. Energy Mater. Sol. Cells 172 (2017) 368–375, https://doi.org/10.1016/j.solmat.2017.08.010.

[25] Y. Zhou, M. Yang, W. Wu, A.L. Vasiliev, K. Zhu, N.P. Padture, Room-temperature crystallization of hybrid-perovskite thin films via solvent–solvent extraction for high-performance solar cells, J. Mater. Chem. A 3 (2015) 8178–8184, https://doi.org/10.1039/C5TA00477B.

[26] C.H. Chiang, Z.L. Tseng, C.G. Wu, Planar heterojunction perovskite/$PC_{71}BM$ solar cells with enhanced open-circuit voltage via a (2/1)-step spin-coating process, J. Mater. Chem. A 2 (2014) 15897–15903, https://doi.org/10.1039/C4TA03674C.

[27] D. Bi, W. Tress, M.I. Dar, P. Gao, J. Luo, C. Renevier, K. Schenk, A. Abate, F. Giordano, J.P. Correa Baena, J.D. Decoppet, S.M. Zakeeruddin, M. K. Nazeeruddin, M. Grätzel, A. Hagfeldt, Efficient luminescent solar cells based on tailored mixed-cation perovskites, Sci. Adv. 2 (2016) 1501170, https://doi.org/10.1126/sciadv.1501170.

[28] Y.C. Kim, N.J. Jeon, J.H. Noh, W.S. Yang, J. Seo, J.S. Yun, A. Ho-Baillie, S. Huang, M.A. Green, J. Seidel, T.K. Ahn, S.I. Seok, Beneficial effects of PbI_2 incorporated in organo- lead halide perovskite solar cells, Adv. Energy Mater. 6 (2016) 1502104, https://doi.org/10.1002/aenm.201502104.

[29] M. Ralaiarisoa, Y. Busby, J. Frisch, I. Salzmann, J.J. Pireaux, N. Koch, Correlation of annealing time with crystal structure, composition, and electronic properties of $CH_3NH_3PbI_3-xClx$ mixed-halide perovskite films, Phys. Chem. Chem. Phys. 19 (2017) 828–836, https://doi.org/10.1039/C6CP06347K.

[30] L. Tian, W. Zhang, Y. Huang, F. Wen, H. Yu, Y. Li, Q. Wang, C. Peng, Z. Ma, T. Hu, L. Du, M. Zhang, Effects of annealing time on triple cation perovskite films and their solar cells, ACS Appl. Mater. Interfaces 12 (2020) 29344–29356. https://pubs.acs.org/doi/10.1021/acsami.0c06558.

[31] G. Li, K.L. Ching, J.Y.L. Ho, M. Wong, H.S. Kwok, Identifying the optimum morphology in high-performance perovskite solar cells, adv. Energy mater. https://doi.org/10.1002/aenm.201401775, 2015, 1401775.

[32] P. Luo, Z. Liu, W. Xia, C. Yuan, J. Cheng, Y. Lu, Uniform, stable, and efficient planar-heterojunction perovskite solar cells by facile low-pressure chemical vapor deposition under fully open-air conditions, ACS Appl. Mater. Interfaces 7 (2015) 2708–2714, https://doi.org/10.1073/pnas.1607850113.

[33] J. Carrillo, A. Guerrero, S. Rahimnejad, O. Almora, I. Zarazua, E.M. Marza, J. Bisquert, G.G. Belmonte, Ionic reactivity at contacts and aging of methylammonium lead triiodide perovskite solar cells, Adv. Energy Mater. 6 (2016) 1502246, https://doi.org/10.1002/aenm.201502246.

[34] J.F. Wang, L. Zhu, B.G. Zhao, Y.L. Zhao, J. Song, X.Q. Gu, Y.H. Qiang, Surface engineering of perovskite films for efficient solar cells, Sci. Rep. 7 (2017) 14478, https://doi.org/10.1038/s41598-017-14920-w.

[35] P.H. Huang, Y.H. Wang, C.W. Huang, W.R. Chen, C.J. Huang, Investigation of inverted perovskite solar cells for viscosity of PEDOT: PSS solution, Crystals 8 (2018) 358, https://doi.org/10.3390/cryst8090358.